Structural "δ Doping" to Control Local Magnetization in Isovalent Oxide Heterostructures

E. J. Moon, Q. He, S. Ghosh, B. J. Kirby, S. T. Pantelides, A. Y. Borisevich, and S. J. May

Structural "Delta-Doping" to Control Local Magnetization in Isovalent Oxide Heterostructures

E. J. Moon,[1] Q. He,[2] S. Ghosh,[3,4] B. J. Kirby,[5] S. T. Pantelides,[3] A. Y. Borisevich,[2] and S. J. May[1,*]

[1] *Department of Materials Science and Engineering, Drexel University, Philadelphia, Pennsylvania 19104, USA*

[2] *Materials Science and Technology Division, Oak Ridge National Laboratory, Oak Ridge, Tennessee 37831, USA*

[3] *Department of Physics and Astronomy and Department of Electrical Engineering and Computer Science, Vanderbilt University, Nashville, Tennessee 37235, USA*

[4] *SRM Research Institute & Department of Physics and Nanotechnology, SRM University, Kattankulathur, 603203 Tamil Nadu, India*

[5] *Center for Neutron Research, National Institute of Standards and Technology, Gaithersburg, Maryland 20899, USA*

* smay@coe.drexel.edu

Modulation and delta-doping strategies, in which atomically thin layers of charged dopants are precisely deposited within a heterostructures, have played enabling roles in the discovery of new physical behavior in electronic materials. Here, we demonstrate a purely structural "delta-doping" strategy in complex oxide heterostructures, in which atomically thin manganite layers are inserted into an isovalent manganite host thereby modifying the local rotations of corner-connected MnO_6 octahedra. Combining scanning transmission electron microscopy, polarized neutron reflectometry, and density functional theory, we reveal how local magnetic exchange interactions are enhanced within the spatially confined regions of suppressed octahedral rotations. The combined experimental and theoretical results illustrate the potential to utilize non-charge-based approaches to "doping" in order to enhance or suppress functional properties within spatially confined regions of oxide heterostructures.

The physical properties of ABO_3-type perovskite oxides are intricately linked to subtle symmetry-lowering atomic displacements, the most notable of which are rotations of the corner-connected BO_6 octahedra [1,2]. These rotations displace the oxygen anions from the face-centered positions, which decreases the B-O-B bond angles and increases the B-O bond lengths. In turn, these structural changes lead to a decrease of the electronic bandwidth and directly modify the electronic and magnetic properties [3]. While the magnitude and symmetry of rotations in bulk compounds are set by the material composition, oxide heterostructures enable the use of interfacial coupling as a means to stabilize non-bulk-like rotations in perovskite epitaxial films and superlattices [4]. Recent studies have established a length scale of < 10 unit cells for the transition region over which the interfacial discontinuity in rotational magnitude and/or pattern is accommodated through spatially varying bond angles and lengths [5-15]. Through the design and control of these interfacial perturbations to atomic structure, substantial changes to electronic and magnetic properties have been induced in ultrathin epitaxial films at the film/substrate interface [16-19]. Interfacial coupling is also operative in superlattices, where the presence of multiple interfaces, a wide array of combinations of constituent materials, and the ability to tune the interfacial distance with respect to the coupling length scale enables new possibilities for structure-based design and control over functional properties [20-24].

In this work, we show how local control of octahedral rotations at the sub-nm length scale can be used to spatially confine enhanced magnetization in manganite superlattices. We demonstrate this approach by inserting ultrathin layers of isovalent but structurally-distinct manganites. This strategy is analogous to delta-doping, in which the insertion of ultrathin impurity layers in a material modifies the local charge density. While delta-doping has been extensively applied to semiconductors and oxides to alter local electronic densities [25-28], the

2

importance of interrelated charge, lattice, and orbital degrees of freedom in complex oxides [29,30] points to non-charge-based local "doping" approaches that are not operative in conventional semiconductors. Here, we demonstrate that the insertion of two unit cells of $La_{0.5}Sr_{0.5}MnO_3$ (LSMO) into thicker $La_{0.5}Ca_{0.5}MnO_3$ (LCMO) layers (20 unit cells) leads to a local reduction of octahedral rotations, while avoiding changes to the nominal Mn valence state due to the isovalent nature of the superlattices. The magnetization within the "doped" regions is enhanced compared to the host layers, consistent with an enhanced ordering temperature in the heterostructure regions with increased Mn-O-Mn bond angles. Density functional theory (DFT) calculations account for the observations and elucidate the local rotation pattern in the LSMO layers, the spatial variation in bond angles, and its effect on local magnetic exchange interactions. The combined experimental and theoretical results illustrate the potential to utilize non-charge-based approaches to "doping" in order to enhance or suppress functional properties within spatially confined regions of oxide heterostructures.

We demonstrate local control of octahedral rotations in $[(LSMO)_n/(LCMO)_{20}]x5$ ($n = 2$, 4) superlattices grown on $La_{0.3}Sr_{0.7}Al_{0.65}Ta_{0.35}O_3$ (LSAT) (001)-oriented substrates, where n indicates thickness in pseudocubic unit cells (uc). The physical idea behind structural "delta-doping" is that the ultrathin LSMO layers exhibit reduced octahedral rotations compared to the surrounding LCMO layers. These LSMO layers create local regions of larger electronic bandwidth and thus greater magnetic exchange interactions [31]. We choose $n = 2$ as the thinnest layer to test this idea as two A-site layers (La,SrO) are needed to fully enclose a MnO_6 octahedron. The two half-doped compounds, $La_{0.5}Sr_{0.5}MnO_3$ and $La_{0.5}Ca_{0.5}MnO_3$, are isoelectronic, thereby mitigating potential effects of charge transfer, allowing us to isolate the effects of structural modulations on the magnetic properties [23]. We use half-doped manganites

3

as this region of the phase diagram hosts competing magnetic and electronic ground states and, as such, physical properties near this composition are highly sensitive to perturbations. Finally, the half-doped composition increases the difference in octahedral rotations between LSMO and LCMO as compared to the more commonly studied $La_{0.7}(Ca,Sr)_{0.3}MnO_3$ doping. In particular, bulk LSMO at half-doping exhibits the $a^0a^0c^-$ rotation pattern (*I4/mcm*) with Mn-O-Mn angles of 169.9° and 180° [32], while half-doped LCMO crystallizes with the $a^-a^-c^+$ pattern (*Pbnm*) with average Mn-O-Mn angles of 160.8° [33]. The difference in octahedral rotations results in a reduction of electronic bandwidth in LCMO compared to LSMO [31], as evidenced by the charge-ordered insulating state in bulk LCMO compared to the competing ferromagnetic/A-type antiferromagnetic phase in LSMO.

The superlattices were grown by oxide molecular beam epitaxy. An ozone/oxygen mixture (~5/95 %) was used as the oxidizing agent at a chamber pressure of ~ 8.5×10^{-6} Torr and a substrate temperature of ~ 600°C. The LSMO layer was first deposited on the LSAT substrate. X-ray reflectivity data measured from the $n = 2$ superlattice are shown in Figure 1(a) and fit well to a model with modulated scattering length density consistent with two unit cells of LSMO within each superlattice period. Corresponding scanning transmission electron microscopy (STEM) high angle annular dark field (HAADF) images are shown in Figure 1(b, c). HAADF and annular bright field (ABF) STEM images were taken using a Nion UltraSTEM operating at 200 kV, equipped with a cold field-emission electron gun and a corrector of third- and fifth-order aberrations. Due to the presence of 50% La ($Z = 57$) and 50% Sr ($Z = 38$) in A-sites, the LSMO layers appear brighter in the HAADF images compared to the LCMO layer, which has 50% La ($Z = 57$) and 50% Ca ($Z = 20$) in A-sites. The lower magnification image [Figure 1(b)] confirms the high quality of the film. The higher magnification image [Figure 1(c)] shows the superlattice

4

has the designed periodicity. A low magnification image of the $n = 4$ superlattice can be found in the Supplemental Material (Figure S1), as can images of defective regions of the samples (Figure S2) [34].
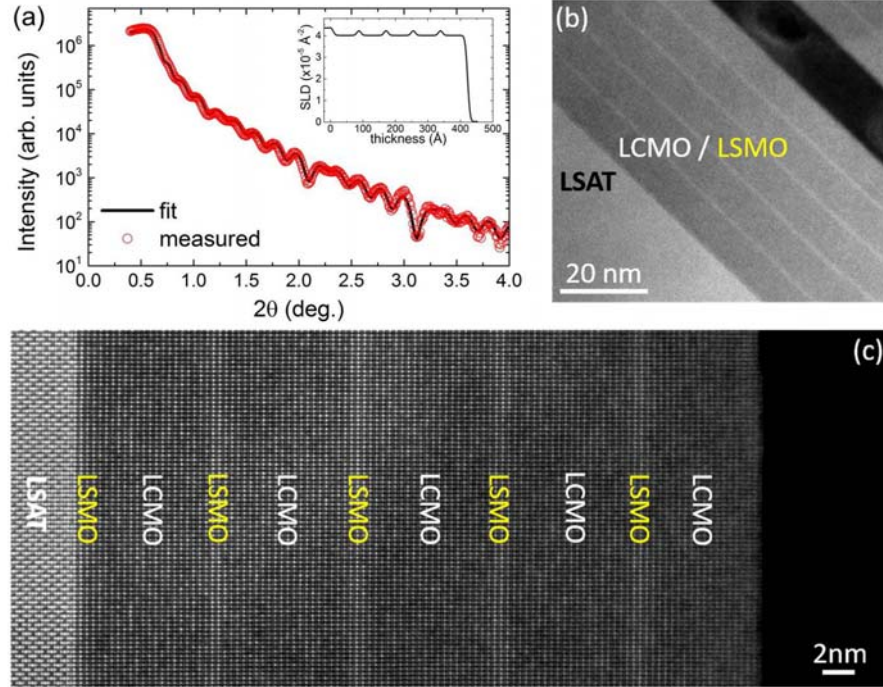

FIG 1. (a) X-ray reflectivity data (red circles) and fit (black line) using GenX software [39] of the $n = 2$ superlattice. Inset: scattering length density profile obtained from the fit. (b) A low magnification STEM-HAADF image of the superlattice. (c) A high magnification STEM-HAADF image of the superlattice, viewed from pseudocubic [110] direction.

Detailed behavior of the MnO_6 octahedra in the superlattice is investigated using STEM annular bright field (ABF) imaging, in which metal cations and oxygen sub-lattices can be directly visualized. We have recently demonstrated, by using STEM-ABF, the full 3D rotation patterns of MnO_6 octahedra can be determined with unit cell resolution [14]. Representative ABF images of the LCMO and LSMO layers are shown in Figure 2(a), viewing along two pseudo-cubic [110] directions ($[110]_{pc}A$ and $[110]_{pc}B$). Using these images, the MnO_6 rotation pattern in

the LCMO layer can be identified as $a^-a^-c^+$, which is consistent with bulk *Pbnm* $La_{0.5}Ca_{0.5}MnO_3$ [33]. In the LSMO layer, the in-plane rotations can be confirmed to be out-of-phase (a^-a^-). However, the nature of the out-of-plane (c-axis) rotation remains ambiguous, possibly due to a small rotation angle. With the in-plane rotation patterns identified, we can further investigate the projected MnO_6 octahedral inclination angle (Φ) across LCMO/LSMO interfaces. Note that Φ is distinct from the Mn-O-Mn bond angle as the projected inclination angle does not capture the magnitude of the oxygen displacement into or out of the image. As shown in Figure 2(b), a suppression of the rotation angles within the LSMO layer is observed, indicating that octahedral rotations can be suppressed over sub-nanometer length scales using this structural "delta-doping" approach. A similar suppression of rotation angles was observed in the $n = 4$ superlattices (Figure S3).
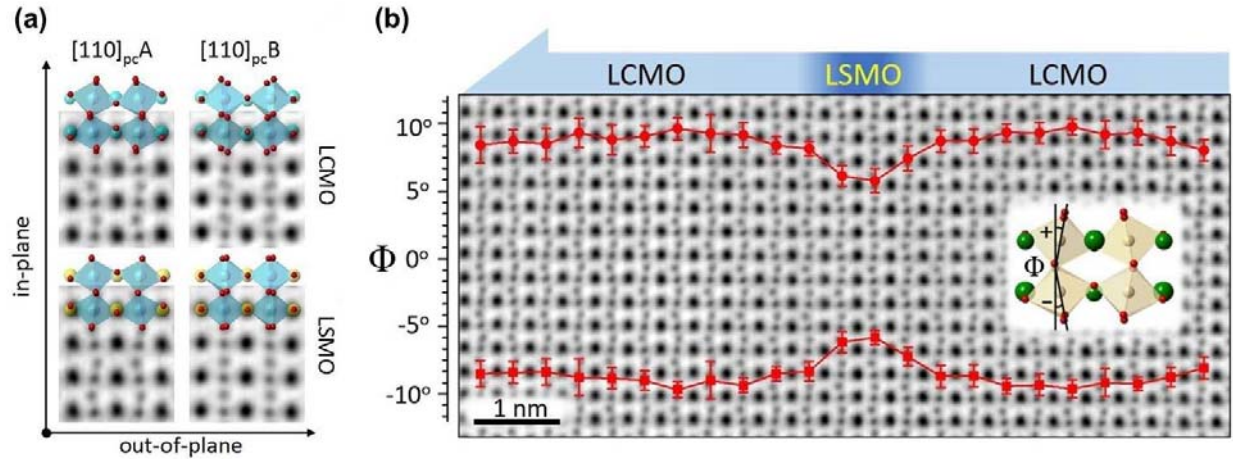

FIG. 2. (a) Representative STEM annular bright field (ABF) images of the LCMO and LSMO layers in the superlattice, viewed from two pseudo-cubic [110] directions that are 90° away ([110]$_{pc}$A and [110]$_{pc}$B). The proposed polyhedral models are shown overlapping the image. (b) The layer-resolved projected inclination angles of the MnO_6 octahedra, viewed from the [110]$_{pc}$A direction, revealing an increased Mn-O-Mn bond angle within the 2-uc LSMO layer. The error bars in (b) indicate the standard deviation obtained from the measurement of inclination angles averaged within each plane.
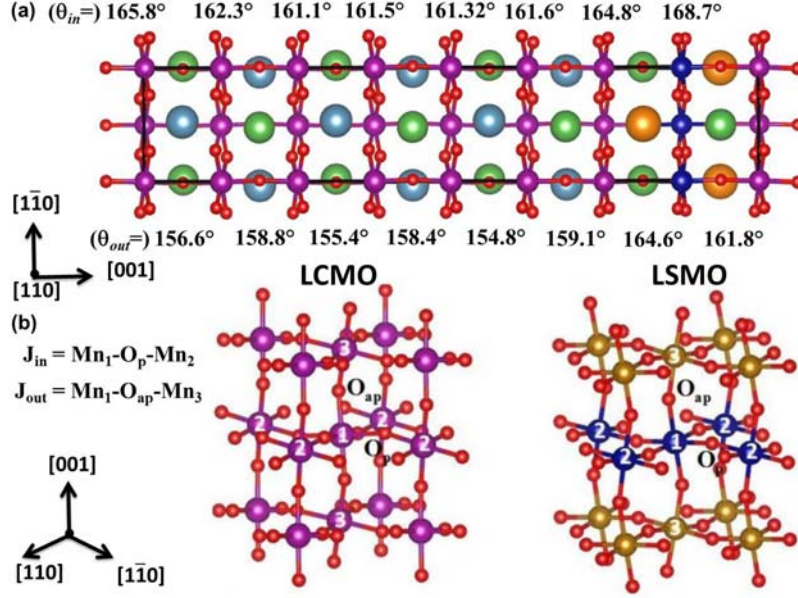
FIG. 3. (a) DFT-optimized structure of a $(LSMO)_2/(LCMO)_6$ superlattice confirms the reduction of the octahedral rotations in the LSMO region. Here, θ_{in} (θ_{out}) indicates the in-plane (out-of-plane) Mn-O-Mn bond angles. (b) In-plane J_{in} (*via* Mn_1-O_p-Mn_2) and out-of-plane J_{out} (*via* Mn_1-O_{ap}-Mn_2) nearest-neighbor isotropic exchange interactions shown for LCMO and LSMO region.

We have performed first-principles density functional theory (DFT) [40] calculations to further elucidate the local rotation pattern in the LSMO layers, the spatial variation in bond angles and its effect on local magnetic exchange interactions. The calculations were carried out projector augmented wave (PAW) potentials [41] as implemented in the Vienna *ab initio* simulation package (VASP) [42]. The exchange-correlation part is approximated by the PBEsol functional [35]. The total energy and Hellman-Feynman forces were converged to 10^{-6} eV and 5×10^{-3} eV/Å, respectively. We have constructed a $\sqrt{2}a_p \times \sqrt{2}a_p \times ma_c$ supercell where a_p is the in-plane lattice constant, a_c is the out-of-plane lattice constant and m represents supercell size along the growth direction. The value of m is 8 and 12 for $(LSMO)_2/(LCMO)_6$ and

(LSMO)$_2$/(LCMO)$_{10}$ superlattices, respectively. We have fixed the in-plane lattice to LSAT (a$_p$ = 3.868 Å) while the out-of-plane lattice and atomic positions are optimized. All calculations were performed with a 500 eV energy cut off and a Γ-centered 4x4x2 K-point mesh. We have considered a (LSMO)$_2$/(LCMO)$_6$ superlattice with the same 50:50 *A*-site cation concentration of La and Ca (Sr) as the experimentally studied superlattices. We impose rock-salt ordering of La and Ca (Sr) throughout the supercell. In the LCMO block, we impose an $a^-a^-c^+$ rotational pattern (similar to bulk LCMO), while, in the 2-uc LSMO block we have separately investigated $a^-a^-c^+$ and $a^-a^-c^-$ patterns. We have considered A-type antiferromagnetism (AF) as the magnetic ordering for both cases. In the fully optimized structures, $a^-a^-c^+$ is found to be 208 meV lower in energy compared to the $a^-a^-c^-$ structure. The optimized structure (LSMO)$_2$/(LCMO)$_6$ is shown in Figure 3(a). We have also considered larger (LSMO)$_2$/(LCMO)$_{10}$ superlattices. In this case, $a^-a^-c^+$ is again found to be the lowest energy structure in the LSMO layers with a 258 meV energy reduction for $a^-a^-c^+$ compared to $a^-a^-c^-$. Further, we have considered other magnetic configurations for both superlattices and found that A-type AF is the lowest magnetic configuration. Hence, DFT calculations show that both LCMO and LSMO regions have an $a^-a^-c^+$ rotation pattern and an A-type AF magnetic configuration.

The depth-dependence of octahedral rotations across the interfaces of the DFT-optimized (LSMO)$_2$/(LCMO)$_6$ structure are also shown in Figure 3(a), separately for in-plane and out-of-plane Mn-O-Mn bond angles, θ_{in} and θ_{out}, respectively. We have divided the (LSMO)$_2$/(LCMO)$_6$ superlattice in three regions as shown in Figure 3(a,b): LCMO (5 layers), LCMO-LSMO interface (2 layers) and LSMO (1 single layer) regions. The average θ_{in} values are found to be 162.4°, 165.3° and 166.7°, for LCMO, interface and LSMO regions, respectively. The average θ_{out} values are found to be 157.3°, 160.6° and 161.8°, respectively for LCMO, interface, and

LSMO regions. The results show that in the LSMO region both θ_{in} and θ_{out} are increased by ~3-5° relative to LCMO. Because the isotropic exchange interactions (J_{ij}) between a pair of Mn ions (Mn_i-O-Mn_j) depend on the oxidation state of the Mn ions and their nearest neighbor environment (local Mn-O-Mn angle and Mn-O distances), the suppression of θ within the LSMO layers has a significant effect on the local magnetism.

We have calculated the ratio of in-plane J_{in} (*via* Mn_1-O_p-Mn_2) and out-of-plane J_{out} (*via* Mn_1-O_{ap}-Mn_3) nearest neighbor exchange interactions for the LCMO and LSMO regions as shown in Figure 3(b) using a method described in the Supplemental Material [34]. The ratios J_{in} (LSMO)/ J_{in} (LCMO) and J_{out} (LSMO)/ J_{out} (LCMO) are found to be 1.8 and 1.5, respectively, indicating an enhancement of nearest-neighbor exchange interactions in the LSMO region compared to the LCMO region. Consistent with the isovalent nature of the superlattice, the calculated local magnetic moment on Mn is ~3.05 μ_B in both LSMO and LCMO throughout the superlattice. The above results suggest an enhancement of the local magnetic interaction and hence an increase of the local ordering temperature (as the magnetic transition temperature is directly coupled to the exchange energy) in the LSMO region, which is purely driven by structural "delta-doping".

In order to confirm the effects of these structural features on the local magnetic properties, polarized neutron reflectometry (PNR) measurements were performed at several temperatures on both the $n = 2$ and 4 superlattices. PNR measurements were carried out on the PBR beamline at the NIST Center for Neutron Research. The films were field-cooled to the measurement temperatures with a 0.5 T field applied in the plane of the films. Measurements were performed in the same field. The results for the $n = 2$ superlattice are shown in Figure 4. The magnetic depth profile was obtained by fitting the PNR data using the NIST Refl1D

software package [43]. In the fits, the nuclear scattering length densities for both LSMO and LCMO were fixed to 3.7×10^{-6} and 3.6×10^{-6} Å^{-2}, consistent with their calculated values, while allowing the magnetization and the thickness of the LSMO and LCMO layers to vary. The fitting parameters were also restricted to ensure that the magnetization (M) does not exceed ~3.7 μ_B per Mn anywhere in the structure, which is only slightly more than the saturation magnetization of bulk LSMO. This set of constraints produces excellent fits to the reflectivity [Figure 4(a)] and spin asymmetry [Figure 4(b)].

The obtained magnetic depth profiles [Figure 4(c)] confirms that the LSMO layers exhibit enhanced magnetization compared to the LCMO layers at all measured temperatures, as would be expected for a sample where the octahedral rotations in LSMO and LCMO differ markedly. The enhanced magnetization is quite narrow in its spatial width, being confined to the two LSMO unit cells. Surprisingly, the depth profile also reveals a staircase-like effect in which the magnetization within both the LSMO and LCMO increases in subsequent layers as the distance from the superlattice/substrate interface increases. It is attributed to a slight change in layer composition as a function of thickness, with from drifts in atomic fluxes during deposition (likely a slight increase of La) or a greater concentration of oxygen vacancies in the near-surface region of the superlattices. As noted earlier, the half-doped composition of the LSMO and LCMO layers marks the boundary between ferromagnetic and antiferromagnetic phases in bulk [32,44], with previous studies showing that the magnetic properties of films change substantially with small changes in doping at this point in the phase diagram [45,46]. As the superlattices are isovalent, the enhanced measured magnetization does not arise from a change in the magnitude of the local Mn moments but instead from either an increase in the magnetic ordering temperature within the LSMO layers or an enhanced double exchange contribution to the

magnetic interactions, leading to greater spin canting and net magnetization. Evidence for an enhanced ordering temperature can be seen in Figure 4(d), which shows the temperature-dependent magnetization of the LSMO and LCMO averaged over all the layers. The ordering temperature of the 2-uc LSMO layers within the superlattice is clearly higher than that of the 20-uc LCMO layers. This feature is consistent with the increase in local Mn-O-Mn bond angles leading to increased magnetic exchange interactions within the LSMO, as obtained from the DFT calculations. Additionally, we note that the average magnetizations obtained from PNR within the LCMO and LSMO layers are less than 0.2 and 0.7 μ_B/Mn, respectively, at 50 K. With the exception of the top LSMO layer, the obtained magnetizations are well below the value of 3 μ_B/Mn that would be expected for ferromagnetic behavior, suggesting that the magnetization within the superlattices comes from a canting of antiferromagnetic order. In contrast, the top LSMO layer exhibits ferromagnetism ($M > 3$ μ_B/Mn at 50 K), which we attribute to either an increased oxygen vacancy concentration or La:Sr ratio within this layer. Similar PNR results were also obtained on the $n = 4$ superlattice, confirming that the enhanced local magnetization from structural delta-doping is reproducible (see Figure S6); however, a direct quantitative comparison between the magnetization of the two superlattices is complicated due to possible extrinsic effects (oxygen vacancies or precise La:Sr stoichiometry) that can also alter the magnetization. We have also attempted to fit the PNR data to a variety of other potential physical scenarios, but alternative models do not reproduce the basic features of the PNR data (see Figure S7).
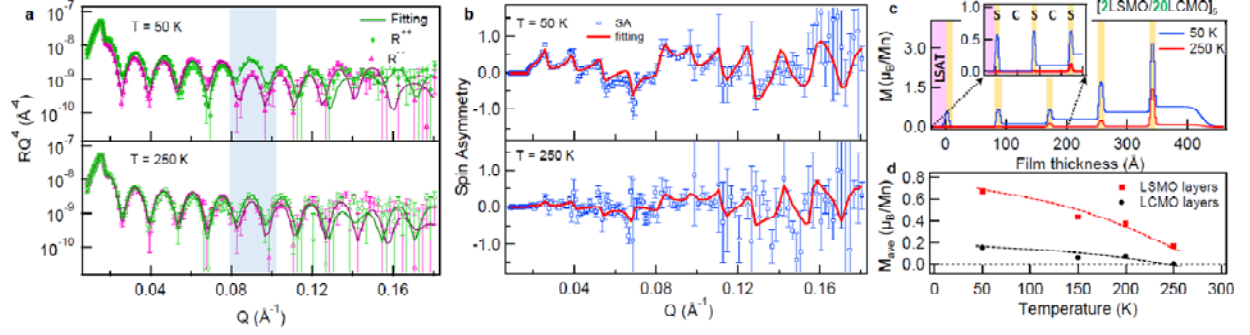
FIG. 4. (a) Polarized neutron reflectivity data and fits multiplied by Q^4 from the n=2 sample obtained at 50 (top) and 250 (bottom) K with a 0.5 T field. Green and magenta symbols indicate the reflectivity measured with neutrons polarized parallel (R^{++}) and antiparallel (R^{--}) to the sample magnetization, respectively. The blue box highlights the superlattice Bragg peak. (b) The corresponding fits (in red) to the spin asymmetry, defined as the difference in R^{++} and R^{--} over the total reflectivity. Error bars in (a) and (b) indicate ±1 standard deviation. (c) Magnetic depth profiles obtained at both temperatures. Orange enclosed regions indicate the 2-uc LSMO layers. The obtained magnetic depth profile demonstrates that the magnetization is enhanced within the LSMO layers which exhibit reduced octahedral rotations but the same Mn valence as the LCMO layers. (d) The average magnetization within the LSMO and LCMO layers as a function of temperature is indicative of a higher Curie temperature within the 2-uc LSMO layers compared to the 20-uc LCMO layers.

These results validate a "delta-doping" approach, based purely on altering local structure, as a means to spatially confine or enhance local magnetic interactions in complex oxide heterostructures. While this work was carried out on manganites near the antiferromagnetic/ferromagnetic phase boundary, we note that physical properties of perovskites that are dependent on electronic bandwidth, most notably magnetism and electronic phase transitions, are directly coupled to octahedral rotations. Therefore, this same design strategy should be operable for perovskites that are ferromagnetic, such as $R_{0.7}Sr_{0.3}MnO_3$ or $R_{0.5}Sr_{0.5}CoO_3$ (where R is a rare earth cation) [31,47,48], or antiferromagnetic, such as $SrMnO_3/CaMnO_3$, $RCrO_3$, or $RFeO_3$-based

superlattices [49,50], as both double-exchange and superexchange are strongly coupled to the local bonding environments. Furthermore, as the Dzyaloshinskii-Moriya (DM) interaction is dependent on the magnitude of octahedral rotations [51], the demonstrated approach may provide a means to tailor local spin textures arising from DM-induced spin canting along the growth direction of oxide heterostructures. The ability to spatially confine magnetic states without altering the local charge density or truncating the crystal offers a new means to study magnetism in the ultrathin two-dimensional limit. While previous efforts to understand magnetism in the two-dimensional regime have largely focused on the study of ultrathin films, such investigations unavoidably introduce significant effects from the free surface or film/substrate interface. The demonstrated structural "delta-doping" keeps the three-dimensional nature of the ABO$_3$ perovskite crystal intact while systematically altering ordering temperatures of buried magnetic layers. Similarly, metal-insulator and charge ordering transitions are dependent on B-O-B bond angles [52,53], allowing for the potential confinement of such electronic phase transitions through local doping of octahedral rotations. We anticipate that this approach will prove enabling in systemically probing the evolution of magnetism or electronic phases as a function of confinement and dimensionality.

* smay@coe.drexel.edu

[1]   A. M. Glazer, Acta. Cryst. B **28**, 3384 (1972).

[2]   P. M. Woodward, Acta. Cryst. B **53**, 32 (1997).

[3]   J. B. Goodenough, Rep. Prog. Phys. **67**, 1915 (2004).

[4]   J. M. Rondinelli, S. J. May, and J. W. Freeland, MRS Bull. **37**, 261 (2012).

[5]   C. L. Jia, S. B. Mi, M. Faley, U. Poppe, J. Schubert, and K. Urban, Phys. Rev. B **79**, 081405(R) (2009).

[6]   A. Y. Borisevich, H. J. Chang, M. Huijben, M. P. Oxley, S. Okamoto, M. K. Niranjan, J. D. Burton, E. Y. Tsymbal, Y. H. Chu, P. Yu, R. Ramesh, S. V. Kalinin, and S. J. Pennycook, Phys. Rev. Lett. **105**, 087204 (2010).

[7]   J. M. Rondinelli and N. A. Spaldin, Phys. Rev. B **82**, 113402 (2010).

[8]   J. He, A. Borisevich, S. V. Kalinin, S. J. Pennycook, and S. T. Pantelides, Phys. Rev. Lett. **105**, 227203 (2010).

[9]   S. J. May, C. R. Smith, J.-W. Kim, E. Karapetrova, A. Bhattacharya, and P. J. Ryan, Phys. Rev. B **83**, 153411 (2011).

[10]   J. Y. Zhang, J. Hwang, S. Raghavan, and S. Stemmer, Phys. Rev. Lett. **110**, 256401 (2013).

[11]   R. Aso, D. Kan, Y. Shimakawa, and H. Kurata, Cryst. Growth Design, **14**, 2128 (2014).

[12]   T. T. Fister, H. Zhou, Z. Luo, S. S. A. Seo, S. O. Hruszkewycz, D. L. Proffit, J. A. Eastman, P. H. Fuoss, P. M. Baldo, H. N. Lee, and D. D. Fong, APL Mater. **2**, 021102 (2014).

[13]   D. P. Kumah, A. S. Disa, J. H. Ngai, H. Chen, A. Malashevich, J. W. Reiner, S. Ismail-Beigi, F. J. Walker, and C. H. Ahn, Adv. Mater. **26**, 1935 (2014).

[14]   Q. He, R. Ishikawa, A. R. Lupini, L. Qiao, E. J. Moon, O. Ovchinnikov, S. J. May, M. D. Biegalski, and A. Y. Borisevich, ACS Nano **9**, 8412 (2015).

[15]   H. Y. Qi, M. K. Kinyanjui, J. Biskupek, D. Geiger, E. Benckiser, H.-U. Habermeier, B. Keimer, and U. Kaiser, J. Mater. Sci. **50**, 5300 (2015).

[16]   E. J. Moon, P. V. Balachandran, B. J. Kirby, D. J. Keavney, R. J. Sichel-Tissot, C. M. Schlepütz, E. Karapetrova, X. M. Cheng, J. M. Rondinelli, and S. J. May, Nano Lett. **14**, 2509 (2014).

[17]   M. D. Biegalski, Y. Takamura, A. Mehta, Z. Gai, S. V. Kalinin, H. Ambaye, V. Lauter, D. Fong, S. T. Pantelides, Y. M. Kim, J. He, A. Borisevich, W. Siemons, and H. M. Christen, Adv. Mater. Interfaces **1**, 1400203 (2014).

[18]   D. Kan, R. Aso, R. Sato, M. Haruta, H. Kurata, and Y. Shimakawa, Nat. Mater. **15**, 432 (2016).

[19]   Z. Liao, M. Huijben, Z. Zhong, N. Gauquelin, S. Macke, R. J. Green, S. Van Aert, J. Verbeeck, G. Van Tendeloo, K. Held, G. A. Sawatzky, G. Koster, and G. Rijnders, Nat. Mater. **15**, 425 (2016).

[20]   E. Bousquet, M. Dawber, N. Stucki, C. Lichtensteiger, P. Hermet, S. Gariglio, J.-M. Triscone, and P. Ghosez, Nature **452**, 732 (2008).

[21]   J. M. Rondinelli and C. J. Fennie, Adv. Mater. **24**, 1961 (2012).

[22]   X. Zhai, L. Cheng, Y. Liu, C. M. Schlepütz, S. Dong, H. Li, X. Zhang, S. Chu, L. Zheng, J. Zhang, A. Zhao, H. Hong, A. Bhattacharya, J. N. Eckstein and C. Zeng, Nat. Commun. **5**, 4283 (2014).

[23]   E. J. Moon, R. Colby, Q. Wang, E. Karapetrova, C. M. Schlepütz, M. R. Fitzsimmons, and S. J. May, Nat. Commun. **5**, 5710 (2014).

[24]   H. Guo, Z. Wang, S. Dong, S. Ghosh, M. Saghayezhian, L. Chen, Y. Weng, A. Herklotz, T. Z Ward, R. Jin, S. T. Pantelides, Y. Zhu, J. Zhang and E.W. Plummer, Proc. Natl. Acad. Sci. U.S.A. in press (2017).

[25]   Y. Kozuka, M. Kim, C. Bell, B. G. Kim, Y. Hikita, and H. Y. Hwang, Nature **462**, 487 (2009).

[26]   B. Jalan, S. Stemmer, S. Mack, and S.J. Allen, Phys. Rev. B **82**, 081103(R) (2010).

[27]   T.S. Santos, B.J. Kirby, S. Kumar, S.J. May, J.A. Borchers, B.B. Maranville, J. Zarestky, S.G.E. te Velthuis, J. van den Brink, and A. Bhattacharya, Phys. Rev. Lett. **107**, 167202 (2011).

[28]   Y. Z. Chen, F. Trier, T.Wijnands, R. J. Green, N. Gauquelin, R. Egoavil, D. V. Christensen, G. Koster, M. Huijben, N. Bovet, S. Macke, F. He, R. Sutarto, N. H. Andersen, J. A. Sulpizio, M. Honig, G. E. D. K. Prawiroatmodjo, T. S. Jespersen, S. Linderoth, S. Ilani, J. Verbeeck, G. Van Tendeloo, G. Rijnders, G. A. Sawatzky and N. Pryds, Nature Mater. **14**, 801 (2015).

[29]   H.Y. Hwang, Y. Iwasa, M. Kawasaki, B. Keimer, N. Nagaosa, and Y. Tokura, Nature Mater. **11**, 103 (2012).

[30]   J. Chakhalian, A. J. Millis, and J. Rondinelli, Nature Mater. **11**, 92 (2012).

[31]   P. G. Radaelli, G. Iannone, M. Marezio, H. Y. Hwang, S.-W. Cheong, J. D. Jorgensen and D. N. Argyriou, Phys. Rev. B **56**, 8265 (1997).

[32]   O. Chmaissem, B. Dabrowski, S. Kolesnik, J. Mais, J. D. Jorgensen, and S. Short, Phys. Rev. B **67**, 094431 (2003).

[33]   P. G. Radaelli, D. E. Cox, M. Marezio, and S.-W. Cheong, Phys. Rev. B **55**, 3015 (1997).

[34]   See Supplemental Material at (url to be inserted) for details of STEM measurements, additional STEM image, results from $n = 4$ superlattice, details of PNR fits, and information on the calculation of exchange energies, which includes Refs. [35-38].

[35]   J. P. Perdew, A. Ruzsinszky, G. I. Csonka, O. A. Vydrov, G. E. Scuseria, L. A. Constantin, X. Zhou, and K. Burke, Phys. Rev. Lett. **100**, 136406 (2008).

[36]   J. P. Perdew, K. Burke and Ernzerhof, Phys. Rev. Lett. **77**, 3865 (1996).

[37]   J. P. Perdew, in *Electronic Structure of Solids '91,* edited by P. Ziesche and H. Eschrig (Akademie Verlag, Berlin, 1991), p. 11.

[38]   B. Hammer, L. B. Hansen, and J. K. Nørskov, Phys. Rev. B **59**, 7413 (1999).

[39]   M. Björck and G. Andersson, J. Appl. Crystallogr. **40**, 1174 (1997).

[40]   W. Kohn and L. J. Sham, Phys. Rev. **140**, A1133 (1965).

[41]   G. Kresse and D. Joubert, Phys. Rev. B **59**, 1758 (1999).

[42]   G. Kresse and J. Furthmüller, Phys. Rev. B **54**, 11169 (1996).

[43]   P.A. Kienzle, K.V. O'Donovan, J.F. Ankner, N.F. Berk, C.F. Majkrzak; http://www.ncnr.nist.gov/reflpak.

[44]   P. Schiffer, A. P. Ramirez, W. Bao, and S.-W. Cheong, Phys. Rev. Lett. **75**, 3336 (1995).

[45]   T. S. Santos, S. J. May, J. L. Robertson, and A. Bhattacharya, Phys. Rev. B **80**, 155114 (2009).

[46]   C. A. F. Vaz, J. A. Moyer, D. A. Arena, C. H. Ahn, and V. E. Henrich, Phys. Rev. B **90**, 024414 (2014).

[47]   I. O. Troyanchuk, N. V. Kasper, D. D. Khalyavin, A. N. Chobot, G. M. Chobot and H. Szymczak, J. Phys.: Conden. Matter **10**, 6381 (1998).

[48]   D. Phelan, Y. Suzuki, S. Wang, A. Huq, and C. Leighton, Phys. Rev. B **88**, 075119 (2013).

[49]   O. Chmaissem, B. Dabrowski, S. Kolesnik, J. Mais, D. E. Brown, R. Kruk, P. Prior, B. Pyles, and J. D. Jorgensen, Phys. Rev. B **64**, 134412 (2001).

[50]   J.-S. Zhou, J. A. Alonso, V. Pomjakushin, J. B. Goodenough, Y. Ren, J.-Q. Yan, and J.-G. Cheng, Phys. Rev. B **81**, 214115 (2010).

[51]   S. Dong, K. Yamauchi, S. Yunoki, R. Yu, S. Liang, A. Moreo, J.-M. Liu, S. Picozzi, and E. Dagotto, Phys. Rev. Lett. **103**, 127201 (2009).

[52]   J. B. Torrance, P. Lacorre, A. I. Nazzal, E. J. Ansaldo, and Ch. Niedermayer, Phys. Rev. B **45**, 8209 (1992).

[53]   T. Takeda, R. Kanno, Y. Kawamoto, M. Takano, S. Kawasaki, T. Kamiyama, and F. Izumi, Solid State Sci. **2**, 673 (2000).